CrossMark

Early Results from GLASS-JWST. II. NIRCam Extragalactic Imaging and Photometric Catalog

Emiliano Merlin[1], Andrea Bonchi[2], Diego Paris[1], Davide Belfiori[1], Adriano Fontana[1], Marco Castellano[1], Mario Nonino[3], Gianluca Polenta[2], Paola Santini[1], Lilan Yang[4], Karl Glazebrook[5], Tommaso Treu[6], Guido Roberts-Borsani[6], Michele Trenti[7,8], Simon Birrer[9,10,11], Gabriel Brammer[12,13], Claudio Grillo[14,15], Antonello Calabrò[1], Danilo Marchesini[16], Charlotte Mason[12,17], Amata Mercurio[18], Takahiro Morishita[19], Victoria Strait[12,17], Kristan Boyett[7,8], Nicha Leethochawalit[7,8,20], Themiya Nanayakkara[21], Benedetta Vulcani[22], Marusa Bradac[23,24], and Xin Wang[25]

[1] INAF Osservatorio Astronomico di Roma, Via Frascati 33, I-00078 Monteporzio Catone, Rome, Italy; emiliano.merlin@inaf.it
[2] Space Science Data Center, Italian Space Agency, via del Politecnico, I-00133, Roma, Italy
[3] INAF—Osservatorio Astronomico di Trieste, Via Tiepolo 11, I-34131 Trieste, Italy
[4] Kavli Institute for the Physics and Mathematics of the Universe, The University of Tokyo, Kashiwa, 277-8583, Japan
[5] Centre for Astrophysics and Supercomputing, Swinburne University of Technology, P.O. Box 218, Hawthorn, VIC 3122, Australia
[6] Department of Physics and Astronomy, University of California, Los Angeles, 430 Portola Plaza, Los Angeles, CA 90095, USA
[7] School of Physics, University of Melbourne, Parkville, VIC 3010, Australia
[8] ARC Centre of Excellence for All Sky Astrophysics in 3 Dimensions (ASTRO 3D), Australia
[9] Kavli Institute for Particle Astrophysics and Cosmology and Department of Physics, Stanford University, Stanford, CA 94305, USA
[10] SLAC National Accelerator Laboratory, Menlo Park, CA 94025, USA
[11] Department of Physics and Astronomy, Stony Brook University, Stony Brook, NY 11794, USA
[12] Cosmic Dawn Center (DAWN), Denmark
[13] Niels Bohr Institute, University of Copenhagen, Jagtvej 128, DK-2200 Copenhagen N, Denmark
[14] Dipartimento di Fisica, Università degli Studi di Milano, via Celoria 16, I-20133 Milano, Italy
[15] INAF—IASF Milano, via A. Corti 12, I-20133 Milano, Italy
[16] Department of Physics and Astronomy, Tufts University, 574 Boston Ave., Medford, MA 02155, USA
[17] Niels Bohr Institute, University of Copenhagen, Jagtvej 128, DK-2200 København N, Denmark
[18] INAF—Osservatorio Astronomico di Capodimonte, Via Moiariello 16, I-80131 Napoli, Italy
[19] IPAC, California Institute of Technology, MC 314-6, 1200 E. California Boulevard, Pasadena, CA 91125, USA
[20] National Astronomical Research Institute of Thailand (NARIT), Mae Rim, Chiang Mai, 50180, Thailand
[21] Centre for Astrophysics and Supercomputing, Swinburne University of Technology, PO Box 218, Hawthorn, VIC 3122, Australia
[22] INAF Osservatorio Astronomico di Padova, vicolo dell'Osservatorio 5, I-35122 Padova, Italy
[23] University of Ljubljana, Department of Mathematics and Physics, Jadranska ulica 19, SI-1000 Ljubljana, Slovenia
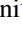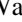[24] Department of Physics and Astronomy, University of California Davis, 1 Shields Avenue, Davis, CA 95616, USA
[25] Infrared Processing and Analysis Center, Caltech, 1200 E. California Blvd., Pasadena, CA 91125, USA

Abstract

We present the reduced images and multiwavelength catalog of the first JWST NIRCam extragalactic observations from the GLASS Early Release Science Program, obtained as coordinated parallels of the NIRISS observations of the Abell 2744 cluster. Images in seven bands (F090W, F115W, F150W, F200W, F277W, F356W, and F444W) have been reduced using an augmented version of the official JWST pipeline; we discuss the procedures adopted to remove or mitigate defects in the raw images. We obtain a multiband catalog by means of forced aperture photometry on point-spread function (PSF)-matched images at the position of F444W-detected sources. The catalog is intended to enable early scientific investigations, and it is optimized for faint galaxies; it contains 6368 sources, with limiting magnitude 29.7 at 5σ in F444W. We release both images and catalog in order to allow the community to become familiar with the JWST NIRCam data and evaluate their merit and limitations given the current level of knowledge of the instrument.

Unified Astronomy Thesaurus concepts: Surveys (1671); Photometry (1234); Galaxies (573); Astronomy image processing (2306)

1. Introduction

The first James Webb Space Telescope scientific images were made available to the public on 2022 July 14. Among them, the GLASS Early Release Science (GLASS-ERS) Program (JWST-ERS-1324, PI Treu; see Treu et al. 2022, T22 hereafter) has obtained the deepest ERS spectro-photometric data, observing the region of the Hubble Frontier Field galaxy cluster Abell 2744 with three instruments. The first GLASS NIRCam data set (see Burriesci 2005; Rieke et al. 2005, for a presentation of the instrument) was obtained on 2022 June 28–29 and it consists of images in seven bands from a parallel pointing of the NIRISS field of view (FoV) on the cluster, with an area of $\sim$9 arcmin^2. The FoV is centered at R.A. $= 3°5017025$, Decl. $= -30°3375436$, i.e., at around one virial radius ($\sim$1–2.5 Mpc) from the cluster center. We refer the reader to Section 6.1 of T22 for full details on the observational setup.

This work is part of a series of short letters illustrating the methods and results from this very first JWST data release. Paper I (Roberts-Borsani et al. 2022) focuses on NIRISS data,

while with this paper we provide the community with an initial release of these NIRCam processed data to allow for early investigation in accompanying first science papers and preparation of future work with NIRCam. This work will also form the basis for a larger and more comprehensive data release when additional NIRCAM imaging is taken for JWST-ERS-1324.

The processing of NIRCam images has been performed with a customised version of the STScI pipeline, adopting the reference and calibration data available at the moment of writing this paper,[26] and is therefore preliminary. This work provides the first users of NIRCam public data with an evaluation of the steps required to reduce the data, the level of uncertainties in their calibration, and initial mitigation strategies for the removal of instrumental defects.

We then used well-tested techniques, inherited from previous projects on deep surveys such as CANDELS (Grogin et al. 2011; Koekemoer et al. 2011; Galametz et al. 2013) and ASTRODEEP (Merlin et al. 2016a, 2021; Castellano et al. 2016), to produce a first photometric catalog, and we are releasing it along with the mosaics of the observed FoV.

We note that modest lensing magnification is expected to be present in the FoV. In this initial set of papers we neglect the effect; the issue will be revisited after the completion of the campaign. However, this has no direct impact on the present work, as we are only releasing measured fluxes.

Despite the mentioned uncertainties, these results provide an illustration of the power of JWST in exploring the distant universe. We expect the quality of the processing to improve over the next few months, thanks to the progress of calibration activities and the refinement of analysis techniques.

This paper is organized as follows. In Section 2 we present the data set and discuss the image processing pipeline. In Section 3 the methods applied for the detection of the sources are described, and in Section 4 we present the photometric techniques used to compute the fluxes. Section 5 lists some known caveats on the accuracy of the catalog, and in Section 6 we summarize the results. Throughout the paper we adopt AB magnitudes (Oke & Gunn 1983).

2. Data Reduction

The present data set consists of seven NIRCam bands images, from 0.9 to 4.4 μm. The FoV is divided in two separated modules. Four images are "short-wavelength": F090W, F115W, F150W, and F200W, with typical native pixels scale close to 0″031, and each module observed with four detectors. The other three are "long wavelength": F277W, F356W, and F444W, with typical native pixel scale close to 0″063, and a single detector per module. We used a customised version of the official STScI JWST pipeline[27] to create mosaics starting from the raw images, with changes motivated by the analysis of tests we performed on simulated data.

We produced the simulations using MIRAGE,[28] a software package that creates synthetic NIRCam raw images with celestial position and depth consistent with the actual

scheduling of the Program as derived from the JWST Astronomer's Proposal Tool. To populate the simulated images, MIRAGE requires an input catalog, which we produced using EGG (Schreiber et al. 2017), a software that uses empirical relations calibrated on the CANDELS data to create mock galaxy catalogs. The sources are simulated as two-component objects, with a bulge and a disk both described by Sérsic (1968) profiles with $n = 4$ and 1, respectively. We also included an additional population of high-redshift galaxies to allow for the study of color selection criteria (see Paper III, Castellano et al. 2022), a stellar field obtained using the TRILEGAL application (Girardi et al. 2005, 2012), and bright stars at the positions of the GAIA sources falling in the FoV to compute the astrometric solution. We used these simulations to prepare the reduction process, introducing some of the improvements described below, and validate the photometric measurement methods.

Real data were then processed as follows. From raw exposures, we used Levels 1 and 2 of the STScI pipeline (see the Appendix in T22) to apply flat-field and dark current correction, and obtain data quality masks (DQM) to identify and potentially flag other detector-level defects. We then applied a number of custom procedures to remove three types of instrumental defects that are not dealt with by the currently available STScI pipeline. Specifically, we have applied corrections for:

1. *1/f noise*, which introduces random vertical and horizontal stripes into the images (see Schlawin et al. 2020). It has been removed by subtracting the median value from each line/column, after masking out all the objects and the bad pixels. The masks have been obtained by running SEXTRACTOR (Bertin & Arnouts 1996) and then dilating the resulting segmentation image by 15 pixels. See the upper panels of Figure 1;

2. *"Snowballs"*, i.e., circular defects that have been observed in after-launch data (see Rigby et al. 2022). These are identified in the DQM, but they are not flagged as "do not use" pixels. Because these defects appear as large clusters of pixels in the DQM, we were able to detect them using again SEXTRACTOR on the DQM itself, setting suitable large threshold areas and retaining only objects with low ellipticity. We have found that an area of 80 pixels is typically effective in identifying 90% of the snowballs in the DQM; we note that this mask is somewhat conservative, as it sometimes identifies regions of unaffected pixels. The masked pixels are excluded from the final sum when creating the scientific mosaic. The procedure is illustrated in the middle panels of Figure 1;

3. *Scattered light/persistence*: as shown in the lower panels of Figure 1, we have found several additive features in F090W and in F115W (in three detectors only, namely a3, b3, and b4). After investigation by JWST technicians during the revision of this paper, it was found out that the issue is due to a so-called "wing-tilt event" that happened during the observations; in practice, a small shift in position of one of the wings of the primary mirror caused the offset/doubling of sources in the data. A full re-observation of the affected bands was approved by the STScI, and the new images will be used for future versions of the catalog. For the present release, we have applied the following procedure to the F090W and

---

[26] The images were initially processed using the files available at the moment of their acquisition, and were reprocessed during the revision of the paper using the new files made available on 2022 July 29 : CAL_VER 1.6.0; CRDS_CTX jwst_0942.pmap.
[27] https://jwst-docs.stsci.edu/jwst-science-calibration-pipeline-overview
[28] https://www.stsci.edu/jwst/science-planning/proposal-planning-toolbox/mirage
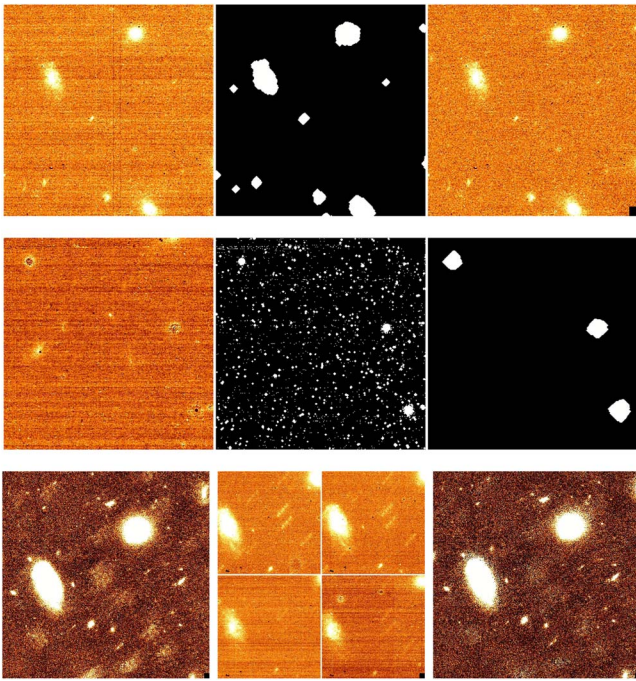
Figure 1. Correction of defects in the raw images. Top panels: effect of the subtraction to remove the $1/f$ noise in both vertical and horizontal directions. Left: original calibrated image; center: dilated mask to remove objects and bad pixels from the estimate of the median row/column level; right: image after noise removal. Middle panels: effect of the method adopted to remove the "snowballs" from the images. Left: original image; center: data quality image as produced by the first two stages of the STScI pipeline. Snowballs are identified as large clusters of pixels typically flagged with value 4. Right: mask obtained by the procedure described in the text. This example is drawn from one image in the F115W filter. Bottom panels: an illustration of the presence of scattered light due to a "wing-tilt" event during observation which caused the offset/doubling of sources in three detectors of the F090W and F115W data, and results of the tentative masking and removal procedure. This example deliberately shows the worst-case scenario, i.e., a portion of the b4 chip in the F090W filter. The effect is much milder or absent in other modules and at wavelengths longer than F150W. Left: mosaic of all F090W images without any masking/removal. Center: individual frames with scattered light patterns. They are more evident in the two longer exposure (upper panels). Right: mosaic of all F090W images after masking of pixels affected by scattered light following the method described in the text.

F115W frames to identify and remove the spurious structures. We run SEXTRACTOR on a median average of the single exposures to obtain a segmentation map containing both real sources and defects, and then on the F444W image where the defects are not present. Cross-correlating the two maps, we were able to single out most of the spurious objects and to mask out their pixels from the final sum, without removing real objects. In the cases where the effect was particularly strong, the final result is a clear improvement of the image quality, even if some residual scattered light is present; see the lower panels of Figure 1.

Clearly, these procedures should be considered as preliminary and temporary means to alleviate these problems, pending definitive solutions that will be implemented in future releases of the STScI pipeline.

The astrometric calibration was performed using SCAMP (Bertin 2006), with third-order distortion corrections (PV coefficients up to $j = 10$), in two steps: first, we aligned the F444W band single exposures to ground-based catalogs (obtained in the i band with the Magellan telescope in good seeing condition, see T22) of the same region, which had been previously aligned to GAIA-DR3 stars (Gaia Collaboration et al., 2022 in preparation); then, we took the resulting high-resolution catalog in F444W as reference for the other JWST bands, using compact, isolated sources detected at high signal-to-noise ratio at all wavelengths. Each NIRCam detector has been analyzed independently, in order to simplify the treatment of distortions and minimize the offsets of the sources in different exposures. The average difference between the positions of bright sources retrieved with SEXTRACTOR runs on each band with respect to the positions in the master catalog used in the SCAMP runs is of $\sim$1 mas, with rms scatter of 15 mas. In some small regions of the short-wavelength images (particularly close to the borders of the detectors) the alignment was suboptimal even after this procedure, so we masked them out from the final mosaics.

We then rescaled the single exposures to units of μJy pixel^{-1}, using the conversion factors outputted by the pipeline. Once again we warn the reader that we used the currently available preliminary calibrations. We checked that the zero-points are reasonable, comparing the measured fluxes of bright sources in four bands (F090W, F150W, F356W, and F444W) with archival ground-based and Spitzer data, finding overall consistency within 0.1–0.2 mag (see Section 4). It is difficult to obtain more precise indications, given the difference in resolution and depth between the instruments. Similar results were obtained by checking the conversion factors given by the pipeline with the reference numbers listed in Table 3 of Rigby et al. (2022). Of course, the zero-points will be calibrated more accurately when updated configuration files are available.

Finally, we used SWARP (Bertin et al. 2002) to combine the single exposures into mosaics projected onto a common aligned grid of pixels, and SEXTRACTOR to further clean the images by subtracting the residual sky background. The pixel scale of all the images was set to $0\rlap.{''}031$ (the approximate native value of the short-wavelength bands), to allow for simple processing with photometric algorithms.

We made a first estimate of the depths of the mosaics by injecting artificial point sources (i.e., point-spread function (PSF) stamps, see below) of known magnitude in empty regions, and measuring their flux and uncertainties with A-PHOT (Merlin et al. 2019), using apertures of radius $0\rlap.{''}1$ as in Table 2 from T22; we found good agreement with their values. We then fine-tuned the rms maps produced by the pipeline, rescaling them by appropriate multiplicative factors (with values ranging from 1.08 to 1.34), to make them fully consistent with the dispersion of the measured fluxes of the artificial sources, which provides an accurate estimate of the real uncertainties including correlated errors between pixels. After this correction, the maximum depths of most of the bands end up being slightly shallower (up to $\sim$0.3 mag) than the ones in T22, while F444W is slightly deeper. In Table 1 we list the final reference depths, estimated as the mode of the limiting total magnitudes (at 5σ in $0\rlap.{''}1$ radius apertures) corresponding to the value of each pixel in the corrected rms maps, along with the total exposure times and the FWHM of the PSF for each band.

Figure 2 shows the final F444W full mosaic, and a small region of the FoV in the seven bands. Clearly, the processing is still not perfect; most noticeably, it shows some residual background features in module a (rightmost in the image). We expect that these features will be further reduced as reference files and pipeline are upgraded. However, we find it good enough to perform a first round of scientific analysis, keeping in mind its limitations. The bottom panels of Figure 2 show the distributions of the values of limiting total magnitude of all
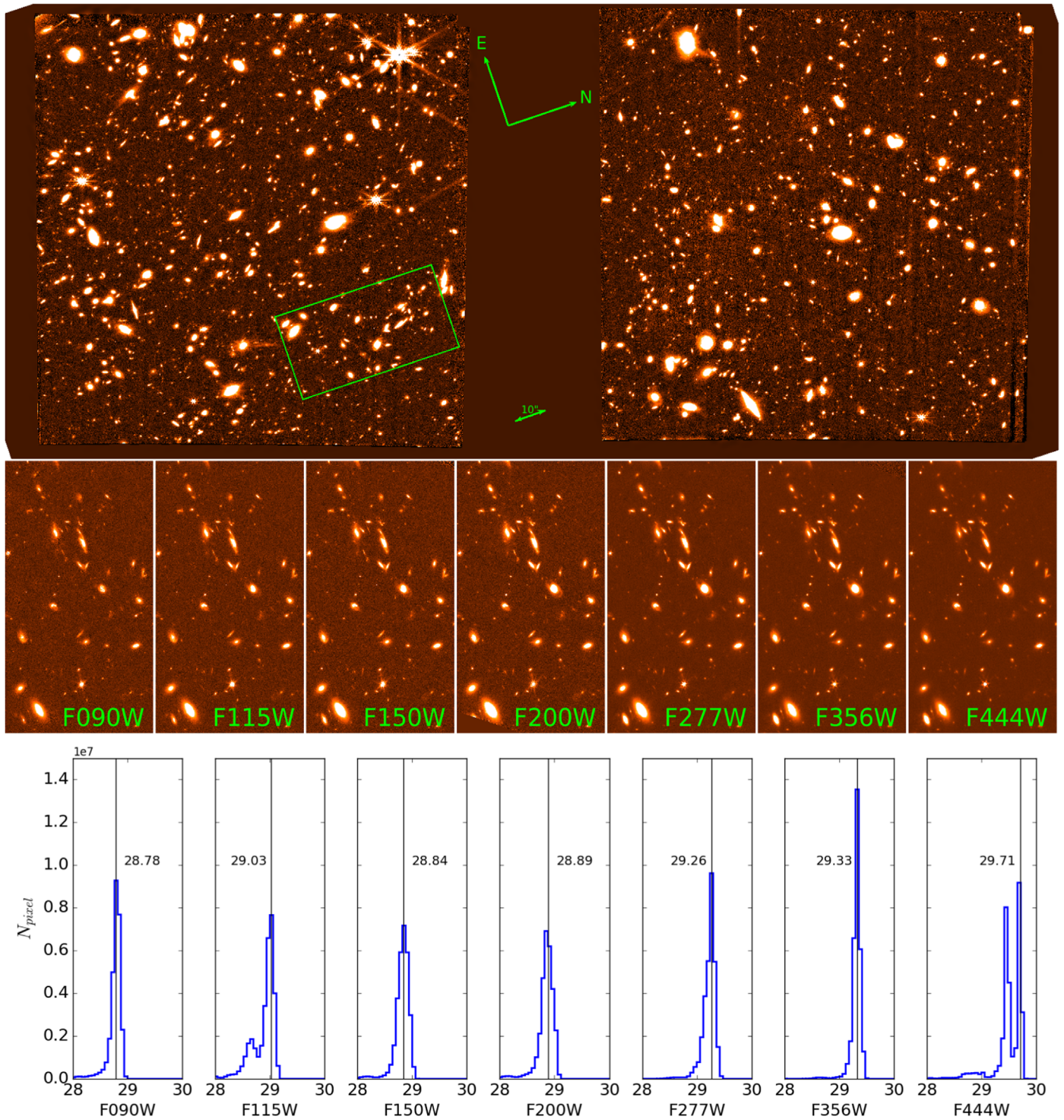
Figure 2. Top panel: full view of the F444W mosaics. Module *b* is shown on the left, module *a* on the right. Middle panels: the small region in the green box of the FoV ($25'' \times 48''$) in the seven observed bands (left to right, F090W, F115W, F150W, F200W, F277W, F356W, and F444W); the color cut is the same in all bands. A three-color composite image of the field is available for download (see Section 6) . Bottom panels: histograms of the 5σ limiting magnitude for all pixels in each mosaic, computed using the rescaled rms maps as described in Section 2. Note the double peak in F444W, caused by the slightly different depth of the two modules.

pixels in each band, computed as described above, and the mode of the distribution.

3. Detection

We performed detection on the F444W band. The reason for this choice is twofold: F444W is the deepest among the seven bands, and high-redshift sources (which are the main targets for this first round of studies) typically have the brightest flux in the reddest band. In contrast, F444W has the broadest FWHM ($0''\!.14$) of the set, so in principle—given the high density of objects—contamination could be an issue. However, visually inspecting the segmentation map, we found that faint objects are typically well-isolated, and confusion is not too significant.

Table 1
Resolution and Maximum Depth of the Seven Bands in the Data Set

Band	FWHM (arcsec)	Exposure Time (s)	Depth (mag)
F090W	0.035	11520	28.78
F115W	0.040	11520	29.03
F150W	0.050	6120	28.84
F200W	0.065	5400	28.89
F277W	0.095	5400	29.26
F356W	0.115	6120	29.33
F444W	0.140	23400	29.71

Note. Depths are 5σ point-source magnitudes in $0''\!.1$ radius apertures.

Table 2
SEXTRACTOR Parameters Used for the Detection Procedure on the F444W Mosaic

Parameter	Value
DETECT_MINAREA	8
DETECT_THRESH	0.7071
ANALYSIS_THRESH	0.7071
DEBLEND_NTHRESH	32
DEBLEND_MINCOUNT	0.0003
BACK_SIZE	64
BACK_FILTERSIZE	3

We used SEXTRACTOR v2.8.6 in the customised version used for the CANDELS campaign (see Galametz et al. 2013), smoothing the scientific image with a Gaussian convolution filter with FWHM $= 0''\!.14$, and applying a detection threshold corresponding to a signal-to-noise ratio (S/N) of 2. This quite aggressive choice was made on the basis of the simulations, to obtain a good balance between completeness and purity. We checked by visual inspection that it allows for the detection of faint sources that are consistently detected also in F356W, without apparently including many spurious ones. We estimated the detection completeness by injecting artificial sources of known magnitude and different morphology (point sources and face-on disks with half-light radii 0.1 arcsec $\leqslant R_h \leqslant$ 1.0 arcsec) in empty regions of the mosaic (to factorize out other selection effects due to, e.g., the choice of detection and deblending parameters), and then running SEXTRACTOR again with the same parameters to check which fraction of them are detected. With this technique we find a completeness of 90% at F444W $= 29.1$, of 75% at F444W $= 29.3$, and of 50% at F444W $= 29.5$ for point sources. The upper panel of Figure 3 shows the completeness for the different classes of injected sources as a function of the input magnitude. On the simulated data, with comparable background levels and the same PSF models, we obtained a purity of $\sim$97% all detections down to the 50% completeness magnitude; we warn that this is an optimistic estimate, considering the many uncertainties and anomalies we found in the real images that were not present in the simulations.

The other parameters used in the run are listed in Table 2 (we include the values for background, which are relevant to the detection process, but we stress that the background subtraction has been performed during image processing as described in Section 2). The final SEXTRACTOR catalog contains 6368 objects. For this first release we did not attempt any cleaning of spurious detections or wrong deblendings.
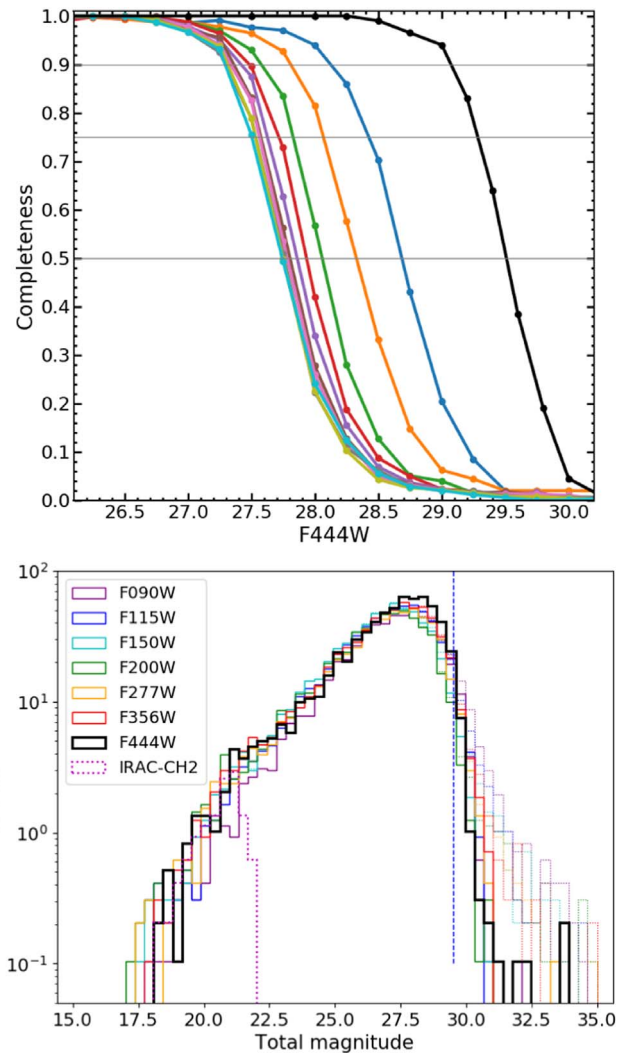

Figure 3. Top panel: detection completeness as a function of the F444W magnitude, estimated by injecting artificial sources in empty regions of the mosaic and detecting with SEXTRACTOR. The colored lines correspond to disks with half-light radii going from 1″ (leftmost cyan line) to $0''\!.1$ (rightmost blue line); the black line is for point sources. Horizontal thin lines mark the 50%, 75%, and 90% completeness levels. Bottom panel: number counts (sources per arcmin^2) of the detected sources, as a function of their measured total magnitude (computed using colors in 2 FWHMs, see Section 4), in all bands. We included all the detections, without attempting to isolate stars or spurious detections, which anyway are a small fraction of the total. The dashed vertical blue line marks the 50% completeness limit in detection. For comparison, we also show the SPITZER IRAC 4.5 μm counts on the same region, obtained by running SEXTRACTOR on the Hubble Frontier Fields images by Lotz et al. (2017).

4. Photometry

To measure the fluxes and colors of the detected objects in all bands, we followed a strategy similar to that adopted for Hubble Space Telescope (HST) images in CANDELS (see, e.g., Galametz et al. 2013) and in ASTRODEEP (Merlin et al. 2016a, 2021). Since the detection band is the one with the coarsest resolution, we PSF-matched all the other images to it for color fidelity. We created convolution kernels using the WEBBPSF models publicly provided by STScI,[29] combining them with a Wiener filtering algorithm based on the one

---

[29] https://jwst-docs.stsci.edu/jwst-near-infrared-camera/nircam-predicted-performance/nircam-point-spread-functions
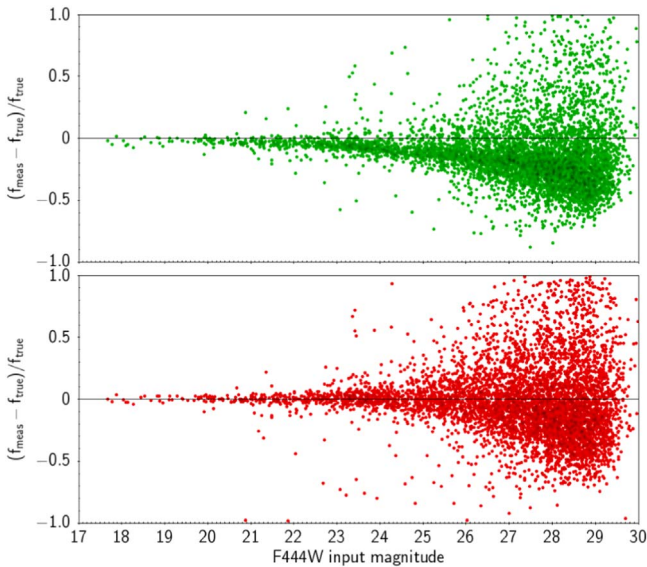
Figure 4. Comparison between SEXTRACTOR FLUX_AUTO (green) and A-PHOT (red) estimated Kron flux on a simulated F444W image; the plots show the relative error with respect to the input (simulated) flux as a function of the input magnitude, and demonstrate that the A-PHOT estimate yields an overall lower median bias.

described in Boucaud et al. (2016); and we used a customised version of the convolution module in T-PHOT (Merlin et al. 2015, 2016b), which uses FFTW3 libraries, to smooth the images. We note that we chose to use these PSFs after trying to create models from the few unsaturated stars available in the fields, using the software GALIGHT (Ding et al. 2020); we checked that the FWHMs of the resulting PSFs were consistent with the those of the WEBBPSF ones, but the resulting convolution kernels were too noisy and yielded more scattered color estimations. The resulting PSF-matched images look good on visual inspection, with no evident signs of artifacts introduced by the procedure, even in the case of the bands with FWHM close to that of F444W. Then, we used A-PHOT to measure the fluxes at the positions of the detected sources on the PSF-matched images, masking neighboring objects using the SEXTRACTOR segmentation map. We measured the flux within the segmentation area (the images being on the same grid and PSF-matched), and the fluxes within six circular apertures with diameters of $0\rlap{.}{''}2$, $0\rlap{.}{''}28$, $0\rlap{.}{''}42$, $0\rlap{.}{''}56$, $1\rlap{.}{''}12$, and $2\rlap{.}{''}24$ (corresponding to 2 to 16 FWHMs).

On the detection image F444W we also estimated a total flux by means of a Kron elliptical aperture (Kron 1980). We point out that while the A-PHOT Kron flux is conceptually identical to the SEXTRACTOR one, we use different parameters, which on the simulated data yielded a smaller median bias at the expense of a slightly larger dispersion. This is shown in Figure 4, where the relative error between measured and input fluxes in a simulated F444W field is shown for both cases. We also want to stress that while the Kron estimate is a good proxy for the total flux of an object, it is prone to errors due to contamination from nearby sources, even after masking them out using the detection segmentation map (because the segmented area typically does not include faint extended wings). Detailed studies focused on individual objects should therefore take this estimate of total fluxes with caution, and perhaps refine the analysis with refined techniques, as done, e.g., with the "GHZ2" object in Paper III (Castellano et al. 2022).

One can then estimate an aperture correction factor for each source from the detection image measurements, $q_{aper} = f_{tot,det}/f_{aper,det}$, and compute its total flux in each band as $f_{tot,band} = q_{aper} \times f_{aper,band}$. We verified on the simulated images that this procedure allows us to obtain a good estimate of the colors, with typical median bias within 5% of the input fluxes. Uncertainties are estimated in the same way, considering the aperture correction factor as a fixed parameter, and thus without propagating the errors on its measurement: $\sigma_{tot,band} = q_{aper} \times \sigma_{aper,band}$. In the released catalog we provide the total fluxes computed using colors in apertures of 2 and 3 FWHMs ($0\rlap{.}{''}28$ and $0\rlap{.}{''}42$ diameter, respectively), and in $0\rlap{.}{''}1$ radius.

The number counts of the detected sources as a function of their measured total magnitude in all bands, computed using the colors in apertures of 2 FWHMs on the PSF-matched images, are shown in the lower panel of Figure 3. The counts are given in arcmin^{-2} using an estimated total area of 9.86 arcmin^2 for the F444W FoV. We also plot the number counts in Spitzer IRAC-CH2 (4.5 μm) from the same area in the Hubble Frontier Fields images (Lotz et al. 2017), for comparison. In Figure 5 we show the S/Ns within apertures of radius $0\rlap{.}{''}1$ of the detected sources, along with the S/N of the artificial point sources used to estimate the depth of the images, as described in Section 2. The S/N of real sources scatters toward lower values because they have different and typically less concentrated light profiles, resulting in varying and typically lower values. The 3σ-clipped median value for real F444W detections is 28.1 at 10σ.

As an external check, and to evaluate the reliability of the current photometric calibration (see Section 2), we compared the magnitudes of the brightest galaxies in our catalog with those from archival data. We considered four bands (Subaru z, VISTA Ks, and Spitzer IRAC CH1 and CH2) with similar wavelength coverage and filter response curves to the NIRCam bands, adding a color correction factor computed by means of theoretical spectral energy distributions (SEDs; using Bruzual & Charlot 2003 models). The results of the test are shown in Figure 6, and confirm an overall good consistency, with median offsets lower than 0.1–0.2 mag (red lines).

5. Caveats

While the GLASS-ERS data set is of exquisite quality, and the photometric techniques adopted in this work have been used and tested extensively on deep HST images in previous surveys, we are aware of some limitations that might affects our results, considering the limited knowledge of the instruments' actual capabilities.

1. As we mentioned several times, the processing of raw data was performed using the currently available versions of pipelines and reference files. We expect the results will significantly improve when updated versions become available;
2. while the background light and many defects have been removed from the images, local variations and residual minor astrometric offsets are still present and can affect the photometry, especially of faint sources;
3. photometric calibration shall be refined, the currently estimated uncertainty being $\sim$0.1–0.2 mag, based on cross-checks with external ground-based catalogs;
4. we did not attempt to remove spurious detections (such as fragments of stellar spikes or pixel clumps at the borders
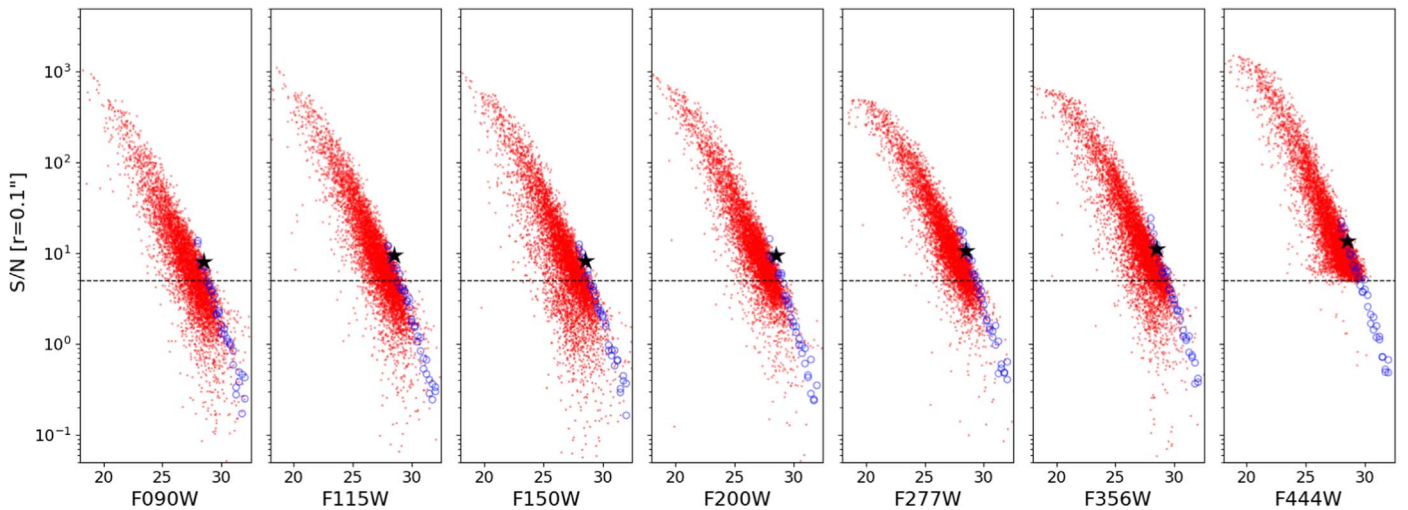
Figure 5. Signal-to-noise ratio in apertures of radius $0.''1$, as a function of the total magnitude, in the seven bands. Red dots: all real detected sources; blue open circles: averages of the artificial point sources injected in the images to estimate depths (see text for details); black star: expected S/N for point sources at mag = 28.5 (based on the JWST Exposure Time Calculator estimates)(https://jwst.etc.stsci.edu/).
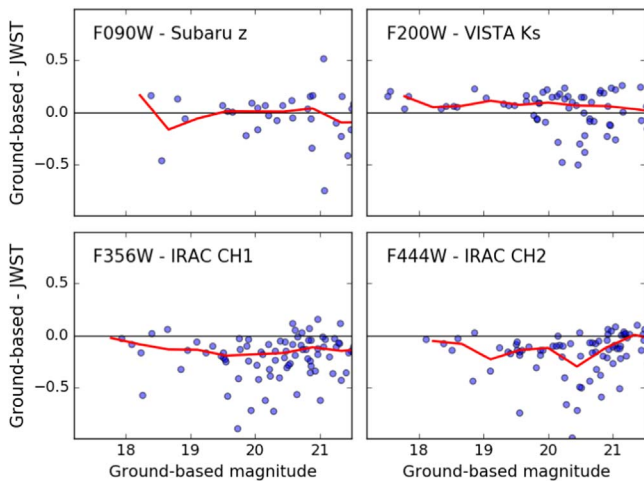

Figure 6. Comparison between NIRCam total magnitudes and catalogs obtained running SEXTRACTOR on archival data, at four wavelengths sampled by similar filters by the JWST and the corresponding instrument (with a color correction applied on the basis of theoretical SEDs). The red lines are the medians of the distributions. The overall consistency is good and the typical average offsets are below 0.1–0.2 mag.

of the mosaics) from the catalog; however, we estimate they contribute to a small fraction of the total detections;

5. WEBBPSF models are an approximate description of the real shape of the observed stars;

6. since aperture photometry is prone to contamination from neighboring sources, estimation of fluxes can be affected, especially in the redder bands where the density of objects is higher and they typically have larger dimensions. We mitigated the issue by masking the image using the segmentation map and choosing relatively small apertures to estimate colors, but a more thorough check should be performed.

6. Summary and Conclusions

We release the images and the corresponding photometric catalog of this very first JWST NIRCam deep extragalactic data, which are used in the accompanying first GLASS science

papers. The images are obtained from the NIRISS parallel pointing of the GLASS-ERS Program; the data set consists of mosaics in seven NIRCam bands (F090W, F115W, F150W, F200W, F277W, F356W, and F444W) with typical depths of $\sim$28.8–29.7 at 5σ (point sources). We processed them using a customised version of the STScI pipeline described in Section 2, to remove defects in the raw exposures and obtain scientific mosaics aligned on a common grid of pixels with scale $0.''031$. We release the images and the corresponding rms maps.

Using SEXTRACTOR we detected 6368 objects on the F444W image, and with A-PHOT we measured aperture photometry on PSF-matched versions of the images. The photometric calibration was checked against ground-based archival data, resulting in an overall accuracy within 0.1–0.2 mag. The released catalog contains coordinates, total fluxes, and corresponding uncertainties of all the detected sources. Fluxes are obtained with the method described in Section 4, i.e., using colors estimated on the PSF-matched images in circular apertures of diameters $0.''28$ and $0.''42$ (corresponding to 2 and 3 FWHMs in F444W), and Kron apertures on the F444W band. The catalog also includes additional quantities of interest measured with SEXTRACTOR on the detection image, such as basic morphological parameters, flags, and `CLASS_STAR`.

Images and catalogs are available for download from the GLASS-ERS collaboration website[30] and from the Astrodeep website.[31] All the JWST data used in this paper can be found in MAST:10.17909/fqaq-p393.

---

[30] https://glass.astro.ucla.edu
[31] https://www.astrodeep.eu

ORCID iDs

Emiliano Merlin ● https://orcid.org/0000-0001-6870-8900
Andrea Bonchi ● https://orcid.org/0000-0002-2667-5482
Diego Paris ● https://orcid.org/0000-0002-7409-8114
Adriano Fontana ● https://orcid.org/0000-0003-3820-2823
Marco Castellano ● https://orcid.org/0000-0001-9875-8263
Mario Nonino ● https://orcid.org/0000-0001-6342-9662
Gianluca Polenta ● https://orcid.org/0000-0003-4067-9196
Paola Santini ● https://orcid.org/0000-0002-9334-8705
Lilan Yang ● https://orcid.org/0000-0002-8434-880X
Karl Glazebrook ● https://orcid.org/0000-0002-3254-9044
Tommaso Treu ● https://orcid.org/0000-0002-8460-0390
Guido Roberts-Borsani ● https://orcid.org/0000-0002-4140-1367
Michele Trenti ● https://orcid.org/0000-0001-9391-305X
Simon Birrer ● https://orcid.org/0000-0003-3195-5507
Gabriel Brammer ● https://orcid.org/0000-0003-2680-005X
Claudio Grillo ● https://orcid.org/0000-0002-5926-7143
Antonello Calabrò ● https://orcid.org/0000-0003-2536-1614
Danilo Marchesini ● https://orcid.org/0000-0001-9002-3502
Charlotte Mason ● https://orcid.org/0000-0002-3407-1785

Amata Mercurio ● https://orcid.org/0000-0001-9261-7849
Takahiro Morishita ● https://orcid.org/0000-0002-8512-1404
Victoria Strait ● https://orcid.org/0000-0002-6338-7295
Kristan Boyett ● https://orcid.org/0000-0003-4109-304X
Nicha Leethochawalit ● https://orcid.org/0000-0003-4570-3159
Themiya Nanayakkara ● https://orcid.org/0000-0003-2804-0648
Benedetta Vulcani ● https://orcid.org/0000-0003-0980-1499
Marusa Bradac ● https://orcid.org/0000-0001-5984-0395
Xin Wang ● https://orcid.org/0000-0002-9373-3865

References

Bertin, E. 2006, in ASP Conf. Ser. 351, Astronomical Data Analysis Software and Systems XV, ed. C. Gabriel et al. (San Francisco, CA: ASP), 112
Bertin, E., & Arnouts, S. 1996, A&AS, 117, 393
Bertin, E., Mellier, Y., Radovich, M., et al. 2002, in ASP Conf. Ser. 281, Astronomical Data Analysis Software and Systems XI ed. D. A. Bohlender, D. Durand, & T. H. Handley (San Francisco, CA: ASP), 228
Boucaud, A., Bocchio, M., Abergel, A., et al. 2016, A&A, 596, A63
Bruzual, G., & Charlot, S. 2003, MNRAS, 344, 1000
Burriesci, L. G. 2005, Proc. SPIE, 5904, 21
Castellano, M., Amorín, R., Merlin, E., et al. 2016, A&A, 590, A31
Castellano, M., Fontana, A., Treu, T., et al. 2022, arXiv:2207.09436
Ding, X., Silverman, J., Treu, T., et al. 2020, ApJ, 888, 37
Galametz, A., Grazian, A., Fontana, A., et al. 2013, ApJS, 206, 10
Girardi, L., Barbieri, M., Groenewegen, M. A. T., et al. 2012, ApSSP, 26, 165
Girardi, L., Groenewegen, M. A. T., Hatziminaoglou, E., & da Costa, L. 2005, A&A, 436, 895
Grogin, N. A., Kocevski, D. D., Faber, S. M., et al. 2011, ApJS, 197, 35
Koekemoer, A. M., Faber, S. M., Ferguson, H. C., et al. 2011, ApJS, 197, 36
Kron, R. G. 1980, ApJS, 43, 305
Lotz, J. M., Koekemoer, A., Coe, D., et al. 2017, ApJ, 837, 97
Merlin, E., Amorín, R., Castellano, M., et al. 2016a, A&A, 590, 30
Merlin, E., Bourne, N., Castellano, M., et al. 2016b, A&A, 595, A97
Merlin, E., Castellano, M., Santini, P., et al. 2021, A&A, 649, A22
Merlin, E., Fontana, A., Ferguson, H. C., et al. 2015, A&A, 582, A15
Merlin, E., Fortuni, F., Torelli, M., et al. 2019, MNRAS, 490, 3309
Oke, J. B., & Gunn, J. E. 1983, ApJ, 266, 713
Rieke, M., Kelly, D., Horner, S. & NIRCam Team 2005, BAAS, 37, 1351
Rigby, J., Perrin, M., McElwain, M., et al. 2022, arXiv:2207.05632
Roberts-Borsani, G., Morishita, T., Treu, T., et al. 2022, arXiv:2207.11387
Schlawin, E., Leisenring, J., Misselt, K., et al. 2020, AJ, 160, 231
Schreiber, C., Pannella, M., Leiton, R., et al. 2017, A&A, 599, A134
Sérsic, J. L. 1968, Atlas de Galaxias Australes (Cordoba: Observatorio Astronomico)
Treu, T., Roberts-Borsani, G., Bradac, M., et al. 2022, ApJ, 935, 110